

Optics Letters

Miniature, sub-nanometer resolution Talbot spectrometer

ERIKA YE, AMIR H. ATABAKI, NINGREN HAN, AND RAJEEV J. RAM*

Massachusetts Institute of Technology, 77 Massachusetts Avenue, Cambridge, Massachusetts 02139, USA

*Corresponding author: rajeev@mit.edu

Received 4 April 2016; revised 27 April 2016; accepted 28 April 2016; posted 28 April 2016 (Doc. ID 262462); published 17 May 2016

Miniaturization of optical spectrometers has a significant practical value as it can enable compact, affordable spectroscopic systems for chemical and biological sensing applications. For many applications, the spectrometer must gather light from sources that span a wide range of emission angles and wavelengths. Here, we report a lens-free spectrometer that is simultaneously compact ($<0.6 \text{ cm}^3$), of high resolution ($<1 \text{ nm}$), and has a clear aperture (of $10 \times 10 \text{ mm}$). The wavelength-scale pattern in the dispersive element strongly diffracts the input light to produce non-paraxial mid-field diffraction patterns that are then recorded using an optimally matched image sensor and processed to reconstruct the spectrum. © 2016 Optical Society of America

OCIS codes: (070.6760) Talbot and self-imaging effects; (120.6200) Spectrometers and spectroscopic instrumentation; (100.3190) Inverse problems.

<http://dx.doi.org/10.1364/OL.41.002434>

Conventional free-space optical spectrometers rely on the dispersion properties of diffractive elements (such as gratings) to separate optical frequencies in the far field. However, to achieve high spectral resolution, the spectrometer must be either large or have a small input aperture that spatially constricts the input light. Therefore, there is a trade-off between resolution, size, and “light-gathering capability” or étendue, which is proportional to the effective area of the aperture and the square of the numerical aperture. As a result, there has been an effort to develop new spectrometers that avoid these constraints. For example, there have been reports of on-chip spectrometers, which have lateral dimensions on the order of hundreds of microns and are high resolution [1–4], but suffer from low étendue due to their small input apertures. A different design uses many filters to spectrally resolve the input signal [4–6]. One can use narrow-band resonant filters to achieve high resolution [4], or broadband filters and employ spectral reconstruction techniques to resolve features smaller than the bandwidth of the filters [5,6]. Another approach that addresses the trade-off between throughput and resolution for conventional diffractive spectrometers is to replace the small input aperture with a so-called “coded aperture,” which allows for an increase in throughput, but requires solving an inverse computational

problem to construct the spectrum [7]. Computational methods are used to spectrally resolve a collimated light source passing through a broadband, high-transmission diffractive element [8]. Similarly, there are reports of computationally reconstructing spectra from speckle patterns of multimode fiber [9,10].

We investigate an alternative spectrometer design that allows us to eliminate the input slit of the dispersive spectrometer and to reduce the spectrometer’s size. Fresnel diffraction from a transmission grating results in a periodic pattern of “self-images,” which are observable starting immediately behind the grating. Halfway between the self-imaging planes are the phase-inverted imaging planes, in which the light and dark regions are swapped. Therefore, the intensity for a point in x and y will alternate from light to dark as one moves away from the grating in z . This repeating pattern was first observed by Talbot and, subsequently, studied by Lord Rayleigh, who proposed that the periodic pattern arose from the interference of the diffracted beams. For weakly dispersive gratings, which satisfy the paraxial approximation, $d \gg \lambda$, the self-images are spaced by the Talbot distance z_T ,

$$z_T = m \frac{2d^2}{\lambda}, \quad (1)$$

where m is an integer corresponding to the interfering diffraction orders, λ is the operating wavelength, and d is the period of the diffraction grating [11]. The Talbot effect can only be observed up to a distance $W / \tan \phi$ behind the grating, where W is the width of the grating and ϕ is the angle of the diffracted beam. Past this distance is the far-field regime, where the diffracted beams no longer overlap.

Since the repeating pattern of “self-images” is (inversely) proportional to the wavelength, the Talbot pattern can be used to perform spectral reconstruction. There have been a few reports of spectrometers of moderate performance that utilize the Talbot effect by measuring the field intensity as a function of distance from the grating [8–12]. Some take the Fourier transform of the periodic pattern to determine the spectrum of the incident light [12–15], while others use the distance from the grating to predict the wavelength [16,17]. To avoid using moving parts to measure the field, one can use digital holography to construct the Talbot pattern [13] or use a tilted detector that can simultaneously measure the field at various distances [14,15]. The experimental resolutions of the fixed-part spectrometers were reported to be 20 [13] and 48 nm [14]. The sizes of the spectrometers were not reported. The first is expected to have dimensions on the order of

tens of centimeters, due to the many optical elements required to build a holographic system. The second is at least 40 mm in length because they use a lens to magnify the self-images onto a detector.

We expand on the basic design presented in [14] and [15]. A 1-D binary transmission grating with period d is positioned such that its grooves are aligned with the y -axis, and the normally incident light propagates along the z -axis [Fig. 1(a)]. The mid-field diffraction pattern is periodic in the x -direction with period d , constant in the y -direction, and periodic in the z -direction with period z_T . A 2-D imager with pixel pitch p is tilted along the z -axis at an angle θ_{det} from the y -axis [Fig. 1(b)], and is used to sample the Talbot diffraction pattern. The spectrometer is shown in Fig. 1(c). In contrast to the Talbot spectrometers presented previously, we (1) utilize the Talbot effect outside the paraxial limit, (2) remove lenses between the grating and image sensor, and (3) optimize the pixel pitch for the grating.

Tilting the imager allows us to sample the diffraction pattern in the z direction, and the spectrum can be obtained by taking the fast Fourier transform (FFT) of the detected Talbot pattern. The length of each pixel in the z direction is $z_{pix} = p \sin \theta_{det}$, and the total distance in z that the imager spans is $z_{spec} = N_Z z_{pix}$, where N_Z is the number of pixels in one dimension of the imager. When $z_{pix} \ll z_T$, the pixels can be modeled as delta functions sampling the Talbot pattern, and the spectrometer's resolution and span are $\Delta k_T = 2\pi/z_{spec}$ and $k_{T,max} = \pi/z_{pix}$, respectively. There is a trade-off between wavelength span and resolution of the spectrometer. Tilting the imager increases resolution because the number of self-images sampled is increased, but also lowers the maximum wavelength that can be detected before aliasing occurs.

The previous reports of Talbot spectrometers, including [14] and [15], only investigated utilizing the Talbot effect under the paraxial limit, where $d \gg \lambda$. The self-images are sharp replications of the grating. However, operation in the paraxial limit constrains the minimum size of the Talbot spectrometer. In the paraxial limit, the Talbot distance can be approximately 100 times larger than the wavelength. Spectral

reconstruction using FFT requires that many periods of the Talbot self-images are sampled by the imager for high spectral resolution. To resolve wavelengths $\delta\lambda$ apart, the minimum distance that the imager needs to sample is approximately $2d^2/\delta\lambda$, according to Fourier theory. A spectrometer with a grating period of $d = 10\lambda$ operating at $\lambda = 500$ nm will need to be at least 5 cm long to have a spectral resolution of 1 nm.

In contrast, we consider a 1-D transmission grating with period $d \sim \lambda$ such that there is significant diffracted power in only the +1, 0, and -1 diffraction orders. The self-images are not sharp replicates of the grating pattern but, instead, are smooth sinusoids [Fig. 1(a)], and appear periodically in z with period [18]

$$z_{SI} = \frac{\lambda}{1 - \sqrt{1 - \frac{\lambda^2}{d^2}}}, \quad (2)$$

and arise from the interference of the -1 and/or +1 diffracted beams with the 0 diffracted beam. In the paraxial limit, this equation simplifies to the Talbot distance in Eq. (1). The wavelength can be calculated from the periodicity of the self-images (z_{SI}).

When operating beyond the paraxial limit, the distance between the self-images is on the order of the wavelength, so a spectrometer of comparable resolution can be 100 times thinner.

To achieve the full potential of the proposed non-paraxial, mid-field spectrometer, an image sensor capable of resolving the self-images without free-space optics is also required. The smallest commercially available imager pixel size is on the order of a micron, larger than the grating period. Therefore, to observe the Talbot effect, the pixel pitch must not be a multiple of the grating period—the imager will be unable to detect a difference in intensity at the self-imaging planes and the phase-inverted self-imaging planes, and the recorded pattern will be constant in z . The Talbot signal will be maximized when the pixel pitch is an odd multiple of half the grating period.

To verify our model, we built and tested spectrometers with two different grating periods and imager pixel pitches, and observed their performance at various tilt angles between the grating and imager. In the first system, we used a transmission phase grating with a grating period of $d = 1.6077$ microns (Ibsen Photonics) and a monochrome CMOS imaging sensor (Aptina MT9P031) with pixel pitch $p = 2.2$ microns, and 2592×1944 pixels (active imager size 5.70 (H) \times 4.28 mm (V)) in size. In the second system (which achieves sub-nanometer resolution), we used a transmission grating with a grating period of $d = 1.035$ microns (Ibsen Photonics) with a monochrome CMOS imaging sensor (Aptina MT9J003) with a pixel pitch $p = 1.67$ microns, and 3872×2764 (active imager size 6.440 mm (H) \times 4.616 mm (V)) pixels in size. As explained in the previous paragraph, the Talbot signal will be greatest for a grating with a period of 1.11 microns, and no Talbot signal will be detected for gratings with a period of 0.835 or 1.67 microns.

Both image sensors incorporate a protective window and microlens array. A commercial readout board (Image Source) is used to capture the sensor data. As no “salt and pepper” pattern is visible in the dark, we suspect that the readout board automatically performs some local averaging to compensate for bad pixels. The readout board is stacked over a miniature USB driver board.

A tunable laser or a fixed wavelength laser is coupled to a single-mode fiber, and the collimated output is passed through a $10 \times$ beam expander (Thorlabs GBE10-B). The final collimated beam is more than 3 cm in diameter, and is normally incident on the grating. To ensure that the imaged area is in the Talbot zone,

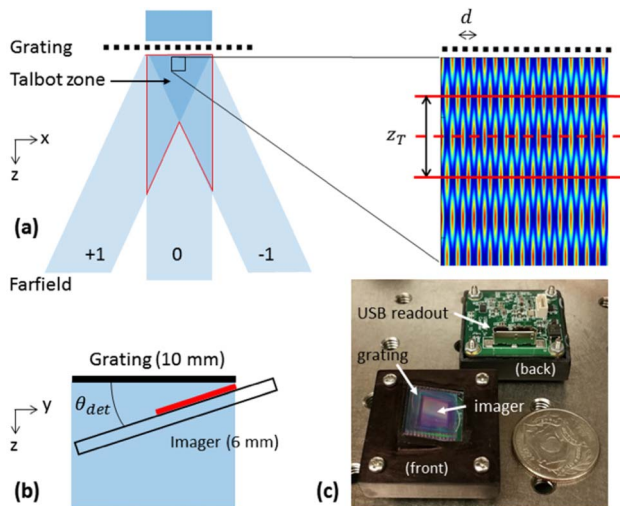


Fig. 1. (a) Illustration of Talbot effect. The self-images are formed in the mid-field where the +1, 0, and -1 diffracted beams interfere. The Talbot pattern shows the self-imaging planes (solid red lines and spaced by z_T) and the phase-inverted self-imaging planes (dashed red line). (b) Illustration showing the position of the imager with respect to the grating. (c) Photograph of the spectrometer next to a quarter.

one edge of the imager is positioned to nearly touch the grating [Fig. 1(b)]. The farthest point of the image sensor was determined to be, by visual inspection, less than 6 mm from the top of the grating surface, even under the most extreme tilt tested (36 deg).

Sample images from the higher resolution system ($d = 1.035$ microns, $p = 1.67$ microns) are shown in Fig. 2 (images labeled “Raw”). The periodic pattern of the self-images can be seen in the raw images. After applying a simple bandpass filter to isolate the dominant frequency component in the 2-D Fourier transform of the image, the self-images can be seen clearly (images labeled “Filtered”). The bandpass filter removes the DC background component and spurious peaks that potentially arise from unwanted artifacts in the imager itself. All images shown are a 50 by 50 pixel subsection of the entire image. To obtain the spectrum, we use a 100 column subsection of the full-length image. We noticed that there are slight shifts in the center frequency of the peak for different columns of the imager, which is likely caused by the wavefront aberration of the input or the non-uniform microlens array across the imager for chief-ray angle correction for imaging application. We take the 1-D FFT of the signal, along each detector column in the subsection, and then take the mean of the magnitude of the FFTs to reduce noise (Fig. 2).

Our experimental results are largely consistent with our theoretical model. However, there are a few issues with the spectra. The first is the presence of two main peaks in the spectra. This can be explained by the rotation of the imaged patterns in the experiments. The diffraction pattern is of the form $\cos(ax)\cos(bz)$. Under the rotation of the imager by a small angle ϕ , the image of the field exhibits two spatial frequencies in the z direction, $b(1 - \phi) \pm a\phi$. Therefore, measuring the signal along the columns of the imager will produce a spectrum with two peaks near the expected wavelength. In our analysis, we use the peak at the shorter wavelength as the main peak because it is closer to the expected wavelength.

Second, the measured wavelength also does not match the operating wavelength of 830.15 nm. This, in part, is due to the

rotation of the observed diffraction pattern as discussed above, but also because of the sensitivity of the peak position to the angle of the incidence of the beam. Accurate detection of the wavelength can be achieved by calibrating the spectrometer, since the offset in predicted wavelength is constant (see Fig. 4).

Lastly, the peaks themselves also exhibit small splitting for low sensor tilt angles. This most likely is because the incident beam is not perfectly normal to the grating. Non-normal incidence in the x -direction would result in slightly different diffraction angles for the $+1$ and -1 beams, which would result in two slightly different z_{SI} when they interfere with the 0th diffracted beam. The $+1$ and -1 beams will also interfere with each other, but the periodicity in z will be much larger than z_{SI} , so it can be ignored. The relationship between the degree of peak splitting and the x -component of the wave vector, k_x , for small angle of incidence, is approximately

$$1 \pm \frac{k_x k_g}{k^2 + k_g^2} = \frac{\lambda_{\pm} + \lambda_p \left(-1 + \sqrt{1 - \frac{\lambda_p^2}{d^2}} \right)}{\lambda_{\pm} \sqrt{1 - \frac{\lambda_p^2}{d^2}}}, \quad (3)$$

where $k_g = 2\pi/d$ is the grating vector, λ_p is the center wavelength, and λ_{\pm} are the wavelengths of the two split peaks. For geometric reasons, θ_{det} affects whether this peak splitting is observed. For small θ_{det} , the imager mostly samples the region where all three diffraction orders (-1 , 0 , and 1) exist, so two z_{SI} are measured, and peak splitting is observed according to Eq. (3). For large θ_{det} , the imager mostly samples regions where two of the three diffraction orders (± 1 , 0) exist. When using a subsection of the image, we measure one z_{SI} and observe no peak splitting. The small splitting of the peaks limits the resolution that can be obtained [see Figs. 2(a) and 3], and will be difficult to avoid experimentally if both -1 and $+1$ diffraction orders exist. In Fig. 2(a), the peaks are split by about 3 nm, which corresponds to an incidence angle of 0.03 deg. However, one could use a modified grating, or operate at a higher incidence angle for which only the 0 and 1 (or -1) diffraction orders exist [Figs. 2(c) and 3].

To further verify our model of the Talbot spectrometer, the peak resolution was measured as a function of θ_{det} . The resolution was determined by finding the full width half-maximum (FWHM) of the peaks. As shown in Fig. 3, the spectrometer system with the larger grating period shows an experimental resolution close to the theoretical resolution. The spectrometer system with the smaller grating period shows the correct trend, but has a lower resolution than expected at low θ_{det} because of peak splitting.

We were able to simultaneously resolve light from two (mutually incoherent) lasers (inset in Fig. 3). We used a fiber coupler to combine light from a fixed wavelength laser operating at 829.95 nm with the tunable laser. The combined light was collimated and passed through the beam expander.

In theory, our spectrometer ($d = 1.035$ microns, $p = 1.67$ microns, $\theta_{\text{det}} = 20$ deg) can measure wavelengths from about 520 nm up to 1.03 microns. The lower bound is the wavelength at which the second diffraction order is present, and the upper bound is the wavelength before which aliasing occurs. We experimentally show that it can achieve an operating span of at least 170 nm (limited by the range of the Ti:sapphire laser at shorter wavelengths and the sensitivity of the imager at longer wavelengths) and a resolution of less than 1 nm. The measured spectra as the laser is tuned from 780 to 950 nm are shown in

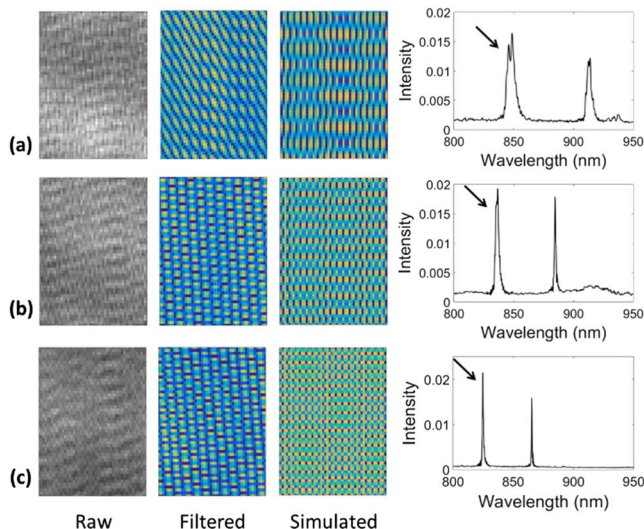


Fig. 2. Raw image, filtered image (using a simple bandpass filter), simulated image, and corresponding spectrum for a spectrometer (for a 100 column subsection) with θ_{det} of (a) 6, (b) 12, and (c) 21 deg. The operating wavelength was 830.15 nm. The arrows point to the peak that we considered to be the “main” peak. In the images, the x - and z - axes are along the rows and columns, respectively.

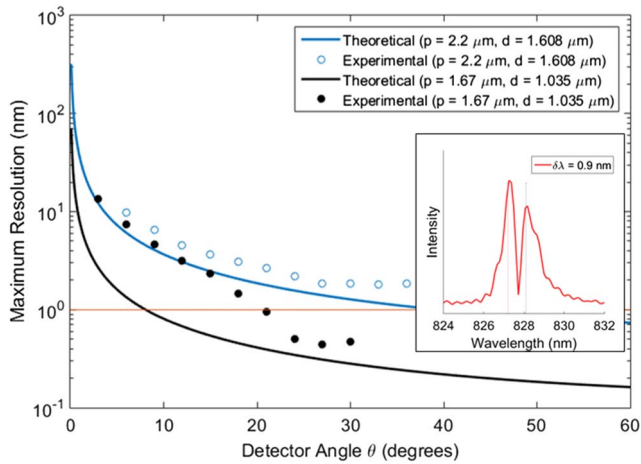


Fig. 3. Theoretical and experimental resolution (FWHM) as a function of detector angle for spectrometer systems 1 and 2 at an operating wavelength of 830.15 nm (inset). Spectrum of two combined laser sources obtained using spectrometer system 2 at $\theta_{\text{det}} = 20$ deg. The lasers are 0.9 nm apart.

Fig. 4. The data were obtained in one sitting to avoid experimental variations in the spectrometer setup.

For the set of data shown, the relationship between the measured wavelength (λ) and laser wavelength (λ_0) is λ [nm] = $0.96\lambda_0$ [nm] + 34 [nm]. The background noise for the 950 nm line is noticeably high because of reduced sensitivity of the imager at longer wavelengths. The background noise for the 820 nm line is high because more signal power is in the spurious peak.

To measure most spectroscopic signals, the Talbot spectrometer needs to have an étendue comparable to that of conventional spectrometers, which are on the order of 10^{-4} to 10^{-3} mm². We expect our spectrometer to have an étendue of 1.3×10^{-4} mm². In this estimation, we used the second (high-resolution) spectrometer with a 21 degree tilt angle, and predicted an acceptance angle tolerance of 0.007 deg in the x -direction and 0.5 deg in the y -direction for 1 nm resolution. This was done by calculating the effect of non-normal

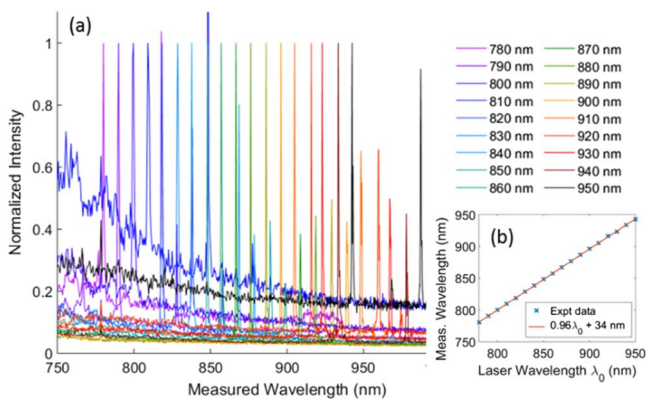


Fig. 4. (a) Measured spectra as the laser is swept from 780 to 950 nm every 10 nm, obtained using a spectrometer with a grating period d of 1.035 microns, a pixel pitch of 1.67 microns, and a grating-to-sensor angle (θ_{det}) of 20 deg. Data are normalized to the bluer peak when the spectra show two peaks. (b) Plot showing linear relation between measured and laser wavelength.

Table 1. Comparison of the Proposed Spectrometer and Commercially Available Products

Spectrometer	Size (mm ³)	Resolution (nm)	Etendue (mm ²)	Bandwidth (nm)
This Letter	10 × 10 × 6	1 nm	1.3×10^{-4}	520–1000
Ocean Optics HR4000	149 × 105 × 45	0.5 nm	3.8×10^{-3}	200–1100
Ibsen EAGLE S	125 × 105 × 45	0.3 nm	2×10^{-3}	822–978
Ibsen FREEDOM	25 × 48 × 16	1.7 nm	2.5×10^{-4}	475–1100

incidence on z_{SI} . Therefore, we expect that the spectrometer proposed in this Letter can be used for most NIR sensing applications, given that the signal is first collimated. A comparison of various spectrometers is presented in Table 1.

Our data demonstrates a functional, sub-nanometer resolution spectrometer with a 10 mm × 10 mm × 6 mm footprint, excluding the readout electronics. This is higher in resolution and smaller in size than the previous Talbot spectrometers, and higher resolution than commercially available free-space diffraction spectrometers of a similar size. The data can be easily extracted by using 1D-FFT, and the 2D imager provides a means of reducing noise by averaging the spectra from multiple columns of the imager. Further performance improvements can be realized by removing the protective window and microlens array, ensuring the alignment of the imager with respect to the grating, calibrating the spectrometer to accurately measure the wavelength, designing the spectrometer such that only the 0 and +1 diffraction orders exist, and using computational methods to correct the peak lineshape as necessary.

REFERENCES

- B. Redding, S. F. Liew, R. Sarma, and H. Cao, *Nat. Photonics* **7**, 746 (2013).
- B. Momeni, E. S. Hosseini, M. Askari, M. Soltani, and A. Adibi, *Opt. Commun.* **282**, 3168 (2009).
- E. le Coarer, S. Blaize, P. Benech, I. Stefanon, A. Morand, G. Lerondel, G. Leblond, P. Kern, J. M. Fedeli, and P. Royer, *Nat. Photonics* **1**, 473 (2007).
- X. Gan, N. Pervez, I. Kyriassis, F. Hatami, and D. Englund, *Appl. Phys. Lett.* **100**, 231104 (2012).
- J. Bao and M. G. Bawendi, *Nature* **523**, 67 (2015).
- Z. Xu, Z. Wang, M. E. Sullivan, D. J. Brady, S. H. Foulger, and A. Adibi, *Opt. Express* **11**, 2126 (2003).
- M. E. Gehm, S. T. McCain, N. P. Pitsianis, D. J. Brady, P. Potluri, and M. E. Sullivan, *Appl. Opt.* **45**, 2965 (2006).
- P. Wang and R. Menon, *Opt. Express* **22**, 14575 (2014).
- B. Redding and H. Cao, *Opt. Lett.* **37**, 3384 (2012).
- B. Redding, S. M. Popoff, and H. Cao, *Opt. Express* **21**, 6584 (2013).
- H. F. Talbot, *Philos. Mag.* **9**(56), 401 (1836).
- A. W. Lohmann, in *Proceedings of the Conference on Optical Instruments and Techniques* (Wiley 1961), p. 58.
- S. De Nicola, P. Ferraro, G. Coppola, A. Finizio, G. Pierattini, and S. Grilli, *Opt. Lett.* **29**, 104 (2004).
- H. L. Kung, A. Bhatnagar, and D. A. B. Miller, *Opt. Lett.* **26**, 1645 (2001).
- H. L. Kung and D. A. B. Miller, "Miniaturized Talbot spectrometer," U.S. patent 65258152 B2 (February 25, 2003).
- G. R. Lokshin, A. V. Uchenov, M. A. Entin, V. E. Belonuchkin, and N. L. Eskin, *Opt. Spectrosc.* **89**, 312 (2000).
- N. Guérineau, E. Di Mambro, J. Primot, and F. Alves, *Opt. Express* **11**, 3310 (2003).
- F. R. S. Lord Rayleigh, *Philos. Mag.* **11**(67), 196 (1881).